Electronic Supplementary Material (ESI) for Journal of Materials Chemistry C.


# Supporting Information

## Revealing Al evaporation-assisted functions in solution-processed ZnO thin film transistors

*By Tae Sung Kang, Tae Yoon Kim, Kap Soo Yoon, Jong Min Kim, Hyun Sik Im, and Jin Pyo Hong**

## 1. Impact of post-annealing temperature on the device output of Al-evaporated ZnO TFTs.

Fig. S1 shows the transfer characteristics of Samples A and C post-annealed between 100-300°C. Annealing of Sample A at higher temperatures led to a higher on-current, as shown in Fig. S1a. In contrast, Sample C prepared in the same range of annealing temperatures showed an improved on-current and higher carrier mobility (Fig. S1b). A plot of the field-effect mobility of Samples A and C versus annealing temperature is shown in Fig. S1c. Sample C had an outstanding carrier mobility with increasing annealing temperature compared to that of Sample A.

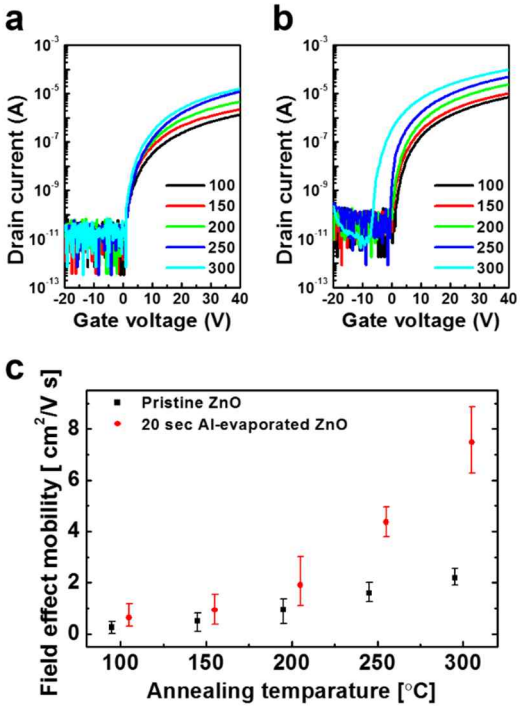


**Fig. S1** Typical transfer characteristics of (a) pristine [Sample A] and (b) optimized 20-sec Al-evaporated ZnO TFTs [Sample B] as a function of annealing temperature ranging from 100 to 300°C. (c) Plots of field-effect mobility versus annealing temperature for both samples.

**2. Output features of pristine and Al-evaporated ZnO TFTs according to Al evaporation time.**

Typical output curves of Samples A, B, and C are presented in Fig. S2. The drain current of Sample A gradually decreased with increasing drain voltage, while no such degradation was observed in the drain currents of Samples B and C, as shown in Figs. S2b and S2c. Degradation in the drain current of Sample A represents the formation of a space charge region arising from spatial charge traps, which is related to the deterioration in carrier mobility of Sample A.

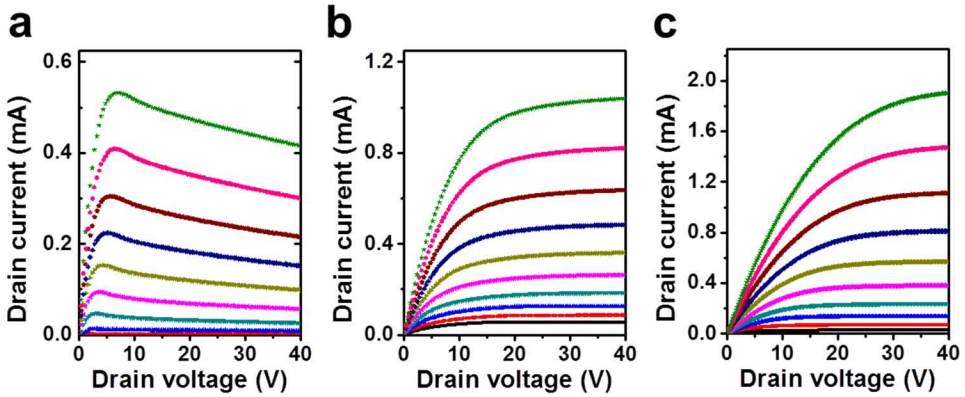


**Fig. S2** Output characteristics of (a) pristine [Sample A], (b) 10-sec Al-evaporated [Sample B], and (c) 20-sec Al-evaporated ZnO TFTs [Sample C] when the gate voltage was varied from 0 to 50 V in steps of 5 V. The length and width of TFTs were 50 and 500 μm, respectively.

**3. AES depth profiles of Al at deposition times of 30 sec and 40 sec.**

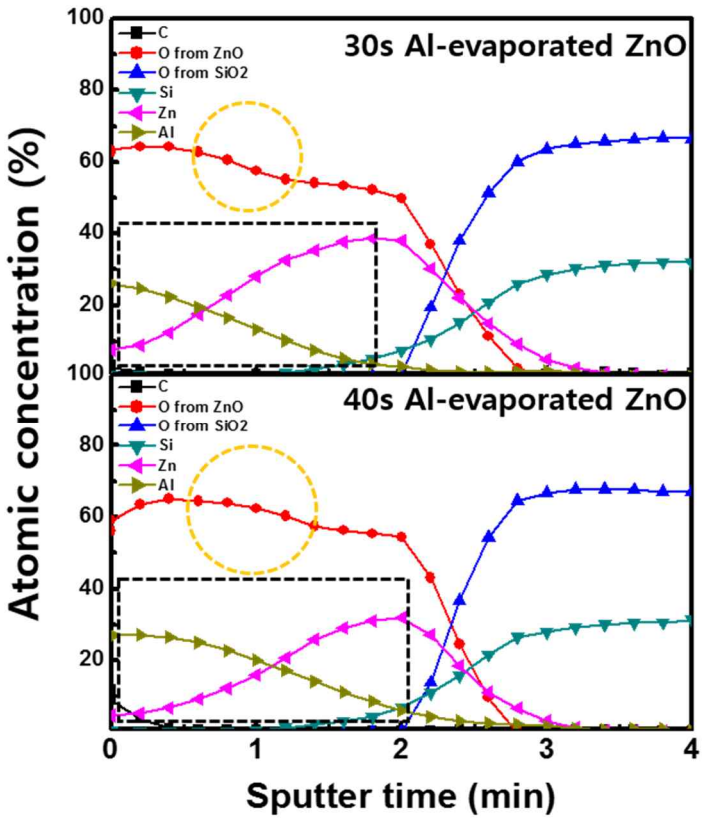


**Fig. S3** AES depth profiles of 30-sec (top) and 40-sec (bottom) Al-evaporated ZnO TFTs. Al diffusion to the ZnO active layer was apparent, as indicated by the black dashed boxes.

**4. HR-TEM images of pristine ZnO and 20-sec Al-evaporated ZnO films.**

Cross-sectional HR-TEM measurements of pristine, 10-sec-, and 20-sec Al-evaporated ZnO layers were conducted. The thicknesses of the pristine and Al-evaporated ZnO layers were 7~8 nm, as seen in Figs. S5a, b, and c. Crystalline SAED patterns are clearly evident in Fig. S5d, indicating the formation of polycrystalline Al-evaporated ZnO layers. No noticeable lattice distortion or migration of the ZnO layers as a result of Al evaporation was observed. In addition, no clear images of Al on the ZnO layers were obtained. This is mainly due to the extremely small amount of Al ions; a 20-sec Al evaporation led to an Al layer only 5~6 Å thick. Therefore, we expect that only small amounts of thermally-activated Al ions can diffuse into the ZnO layer and function as oxidation elements during Al evaporation.

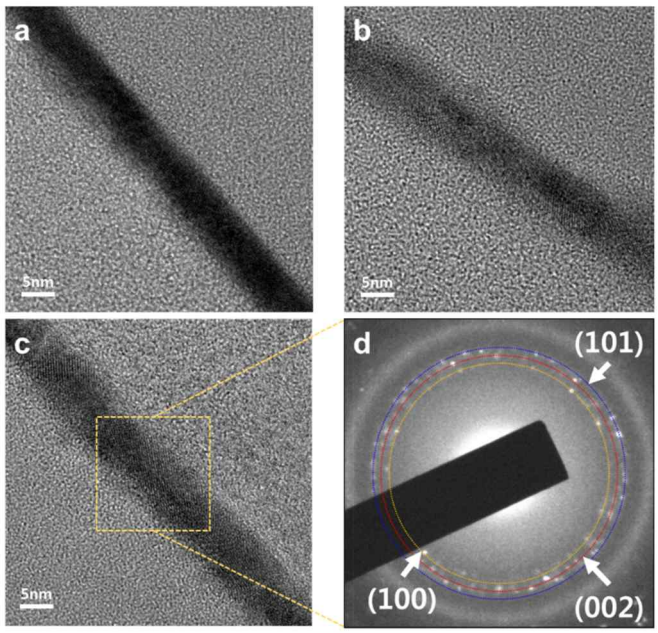


**Fig. S4 C**ross-sectional high-resolution transmission electron microscopy (HR-TEM) images of (a) pristine, (b) 10-sec Al-evaporated, and (c) 20 sec-Al-evaporated ZnO films. (d) Selected area electron diffraction (SAED) patterns of 20-sec Al-evaporated ZnO.

## 5. Energy dispersive X-ray spectroscopy (EDS) analysis of Al-evaporated ZnO

Fig. S5 shows the energy dispersive X-ray spectroscopy (EDS) depth profiles of the 20-sec Al-evaporated ZnO layer, demonstrating the clear presence of Al, Zn, and O elements within the ZnO active layer due to Al ion diffusion during Al evaporation.

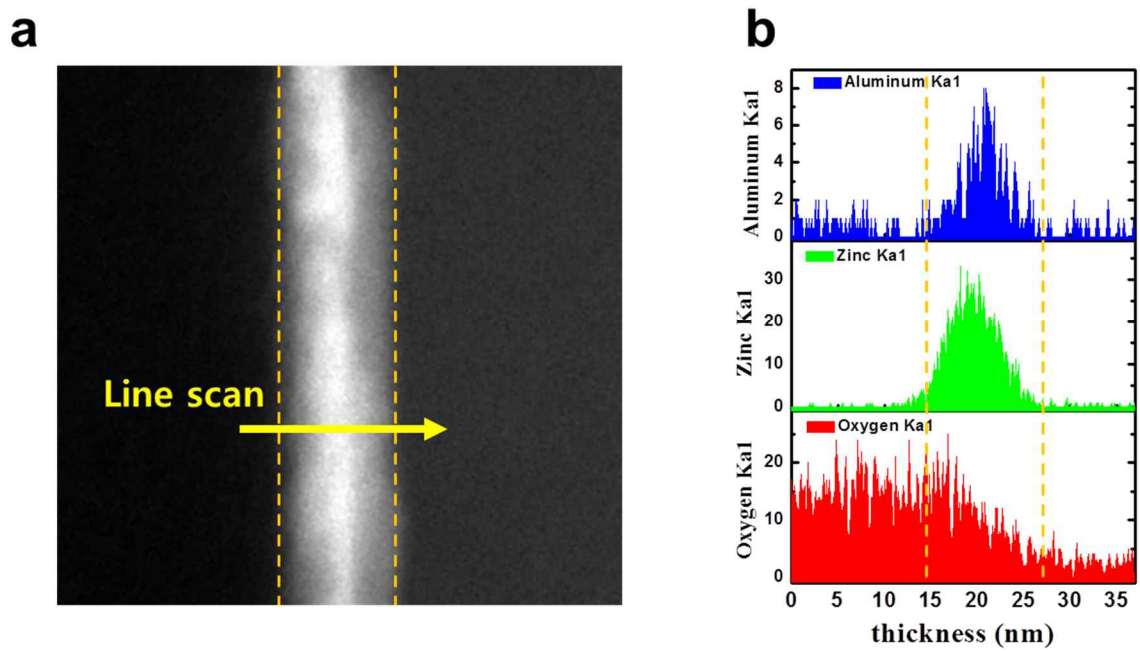


**Fig. S5** (a) Cross-sectional STEM-HAADF view with the line scan region marked in the image, and (b) atomic depth distributions along the line scan of the 20-sec Al-evaporated ZnO film, revealing the clear presence of Al, Zn, and O elements in the ZnO active layer.

## 6. Transfer curves and possible mechanism sketches of single- and double-layered Al-evaporated ZnO TFTs

Fig. 6Sa shows transfer curves of the pristine and Al-evaporated ZnO TFTs, confirming the enhancement in device performance after Al evaporation. Transfer characteristics of single- and double-layered ZnO TFTs, where the latter consists of the same two ZnO active layers, are plotted in Fig. 6Sb. As seen in this figure., the double-layered ZnO TFT had a degraded subthreshold. This result reflects the presence of increased defect sites at the additional interface between the two ZnO active layers, which hindered electron transport.

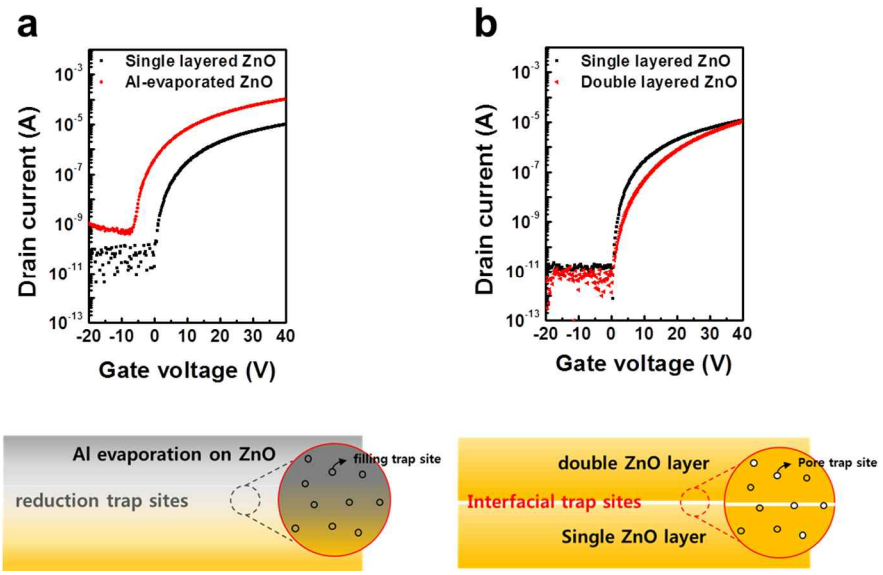


**Fig. S6** Transfer characteristics of (a) pristine (black line) and Al-evaporated (red line) ZnO TFTs, depicting the reduction of trap sites as a result of Al evaporation on the back channel surface (bottom, right). (b) Comparison of electrical characteristics between single- (black line) and double-layer (red line) Al-evaporated ZnO TFTs. The drain voltage ($V_{ds}$) was 10 V at various gate voltages ($V_{gs}$) ranging from -20 to 40 V. Double-layer Al-evaporated ZnO TFTs had relatively deteriorated I-V features compared to those of single-layer Al-evaporated ZnO TFTs due to the presence of interfacial trap sites (bottom, left) between the two active layers.

## 7. Operational stabilities of Al metal-evaporated and $Al_2O_3$-passivated ZnO TFTs

Results of a stability test of Samples B, C, and D under continuously repeated measurements are plotted in Figs. S7a, b, and c, respectively. Transfer characteristics of the 2-nm-, 4-nm-, and 6-nm-thick $Al_2O_3$ film-passivated ZnO TFTs are shown in Figs. 7Sd, e, and f, respectively. As seen in this figure, Al-evaporated ZnO TFTs demonstrated highly stable repeated transfer features. In contrast, when $Al_2O_3$ thin films possibly functioning as insulating layers were deposited on solution-processed ZnO films using an atomic layer deposition process, the $Al_2O_3$-capped ZnO TFTs showed increased negative shifts of threshold voltage and elevated off-current levels under repeated measurements. This metallic conduction behavior of the $Al_2O_3$-capped ZnO TFTs may be due to the enhanced diffusion of Al into the ZnO active layer with increasing $Al_2O_3$ capping layer thickness. As a consequence, the amount of defect-related oxygen in the $Al_2O_3$ layer increases, providing large leakage current paths near the surface of the $Al_2O_3$-capped ZnO active thin layer.

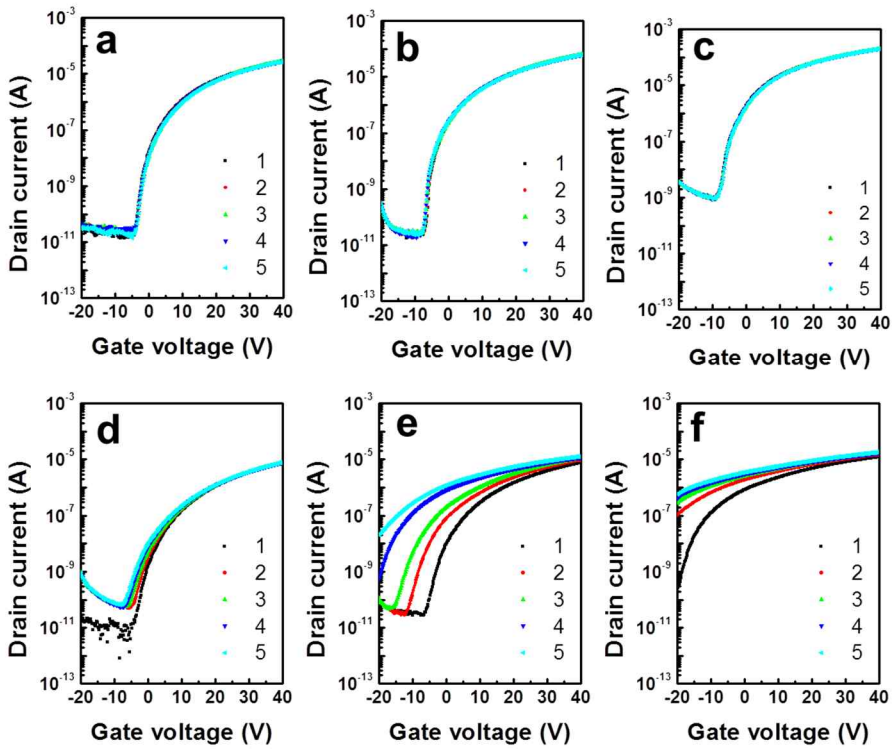


**Fig. S7** Continuously repeated transfer traces of (a) 10-sec, (b) 20-sec, and (c) 30-sec Al metal-evaporated ZnO TFTs. Transfer curves of (d) 2-nm-, (e) 4-nm-, and (f) 6-nm-thick $Al_2O_3$ -passivated ZnO TFTs. All measurements were consecutively repeated five times.

**8. Arrhenius plots of log Id vs. 1000/T in the sub-threshold and above-threshold regions.**

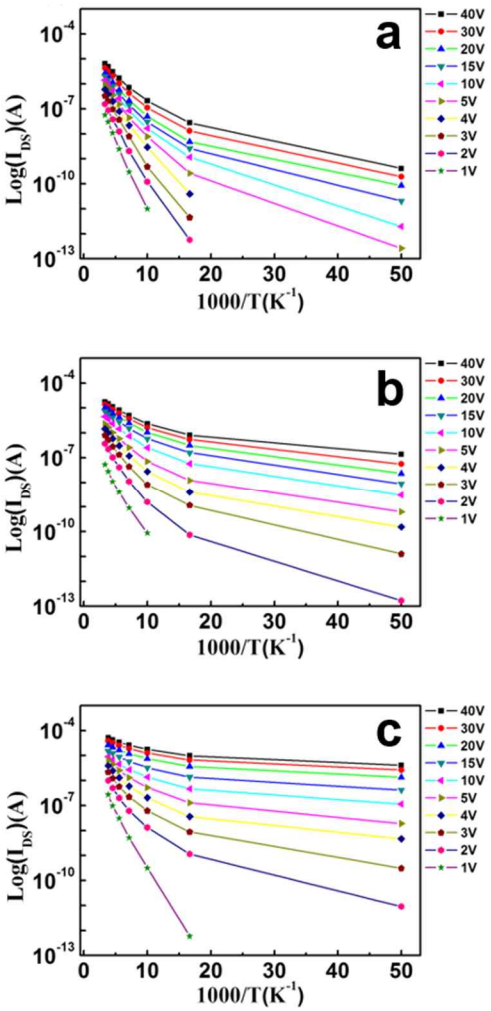


**Fig. S8** Temperature dependence of drain currents on the log scale for (a) pristine, (b) 10-sec Al-evaporated, and (c) 20-sec Al-evaporated ZnO TFTs monitored at various gate voltages at temperatures ranging from 300 to 20 K.

**9. Positive stress test for pristine ZnO TFTs and 20-sec Al-evaporated ZnO TFTs.**

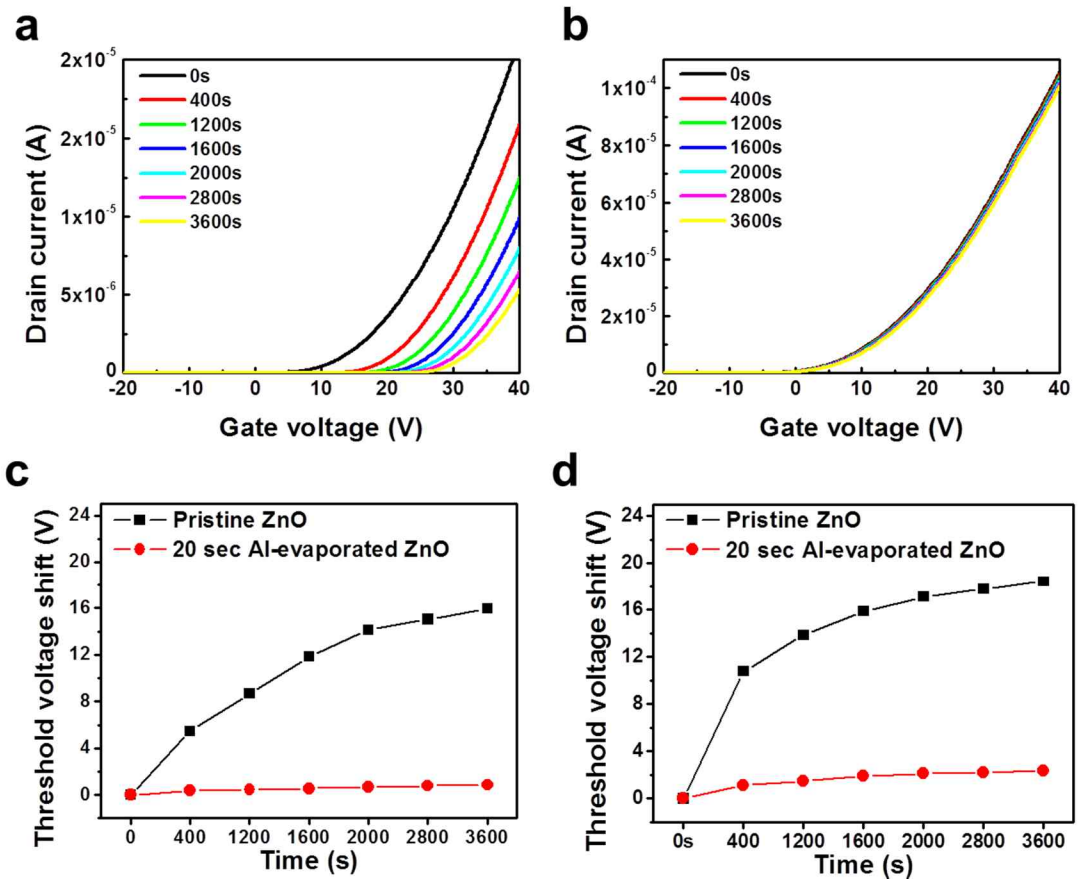


**Fig S9** Transfer characteristics of (a) pristine and (b) 20-sec Al-evaporated ZnO TFTs under positive bias stress (PBS) for 3600 seconds. Threshold voltage shifts of the pristine ZnO (Black line) and 20-sec Al-evaporated ZnO (Red line) TFTs as a function of stress duration time under (c) PBS and (d) PBTS.